Tilt-induced instability of a stratified vortex

NICOLAS BOULANGER, PATRICE MEUNIER
AND STÉPHANE LE DIZÈS

Institut de Recherche sur les Phénomènes Hors Équilibre, 49, rue F. Joliot-Curie, BP 146,
F-13384 Marseille cedex 13, France

This experimental and theoretical study considers the dynamics and the instability of a Lamb–Oseen vortex in a stably stratified fluid. In a companion paper, it was shown that tilting the vortex axis with respect to the direction of stratification induces the formation of a rim of strong axial flow near a critical radius when the Froude number of the vortex is larger than one.

Here, we demonstrate that this tilt-induced flow is responsible for a three-dimensional instability. We show that the instability results from a shear instability of the basic axial flow in the critical-layer region. The theoretical predictions for the wavelength and the growth rate obtained by a local stability analysis of the theoretical critical-layer profile are compared to experimental measurements and a good agreement is observed. The late stages of the instability are also analysed experimentally. In particular, we show that the tilt-induced instability does not lead to the destruction of the vortex, but to a sudden decrease of its Froude number, through the turbulent diffusion of its core size, when the initial Froude number is close to 1. A movie is available with the online version of the paper.

1. Introduction

The presence of intense and small vortices in geophysical flows is problematic for the oceanic and atmospheric models. These structures are unresolved when they become smaller than the mesh size used in the numerical codes, although they might influence the stability and mixing properties of larger scales. In this paper, we consider the stability and dynamics of such an intense vortex when its axis is slightly tilted with respect to the direction of stratification.

In the atmosphere, the large-scale structures (of a few thousand kilometres), created by the baroclinic instability, have a very small Froude number and a small Rossby number. These primary structures are mainly two-dimensional and not likely to be subject to a three-dimensional instability. However, they can be unstable with respect to two-dimensional instabilities (Nieman, Shapiro & Fedor 1993) and create secondary vortices with a smaller length scale (Polavarapu & Peltier 1993; Garnier, Métais & Lesieur 1996). These intense vortices can reach a size of 10 km, which gives a Rossby number of order 10 and a Froude number of order 1. This paper will focus on this type of intense vortex in which the stratified effects are comparable to advection, and in which the effect of the global rotation can be neglected. Our goal is to show that a weak inclination of the vortex can strongly affect its dynamics.

In oceans, vortices are often observed beyond coastal tips or behind islands. They are generated by the tide or strong currents. These vortices are usually inclined with respect to the stratification owing to the slope of coastal regions (see for instance Pawlak *et al.* 2003). When their Froude number is larger than 1, they will be subject
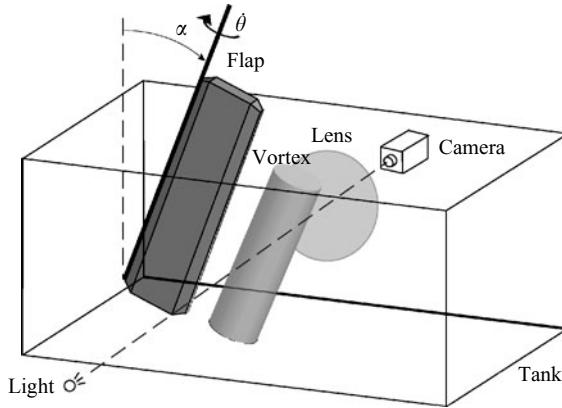
FIGURE 1. Schematic of the experimental set-up. The rotation of the grey plate around its upper edge generates a vortex inclined with respect to the vertical with an angle α. The light, lens and camera allow shadowgraph visualizations.

to the instability described in this paper. However, Coriolis effects might be expected for these vortices since the Rossby number is of order 1 here.

In Boulanger, Meunier & Le Dizès (2007), the structure of a tilted vortex was studied experimentally and theoretically in the limit of small inclination angles. When the Froude number is larger than 1, a critical layer was shown to appear at the radius where the angular velocity of the vortex equals the Brunt–Väisälä frequency. In the viscous regime, this creates a strong vertical motion of order $Re^{1/3}$ in a layer of thickness scaling as $Re^{-1/3}$.

As far as we know, no stability analysis of such a tilted vortex has been performed. However, the effect of a stable stratification on various instabilities has been extensively studied. In the case of several vortices, the stratification stabilizes the elliptic instability (Kerswell 2002) and transforms the Crow instability (Crow 1970) in a so-called zig-zag instability (Billant & Chomaz 2000). For a single vortex, the two-dimensional shear instability and the centrifugal instability are not affected by a stable stratification in the inviscid limit (Hopfinger & van Heijst 1993). However, Cariteau & Flór (2003) reported a new columnar instability of a stratified vortex, which creates some vertical motion in a thin rim around the vortex and leads to a three-dimensional instability. Although they did not add any intentional tilting of the vortex (Cariteau 2005), we will show that this instability is probably due to a weak misalignment of the vortex with the stratification. This previous experimental evidence indicates that this instability is very strong and can be effective even in the presence of very weak tilt angles.

The paper will be organized as follows. In §2, we describe the experimental set-up and the two-dimensional base flow of a tilted vortex. In §3, we show experimental evidence of this new instability, followed by a local theory in §4. The late stages of the instability are considered in §5, before the conclusion in §6.

2. Experimental set-up and base flow

2.1. *Experimental details*

The experimental set-up (figure 1) is explained in detail in Boulanger *et al.* (2007) and only the main features are recalled here. The experiments are performed in a 150 cm
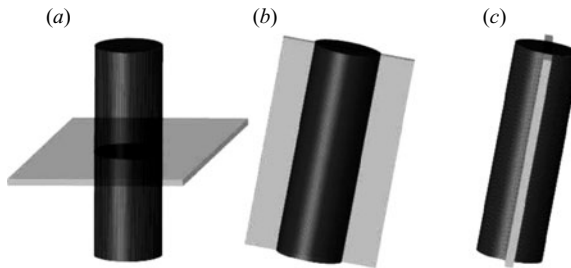
FIGURE 2. Location of PIV measurement planes. (*a*) Transverse plane (*b*) vertical longitudinal plane $\theta = 0$, and (*c*) tilted longitudinal plane, $\theta = \pi/2$.

long, 75 cm wide and 50 cm high Plexiglas tank, filled with a linearly stratified fluid (made using the two-tank method). The density gradient is deduced from density measurements of small samples of fluid every 5 cm, using a densitometer Anton Paar DMA 35N with an accuracy of 10^{-4} kg l^{-1}. By varying the effective depth of fluid between 20 cm and 45 cm and the maximal density between 1.1 and 1.19 kg l^{-1}, we have been able to obtain a Brunt–Väisälä frequency ranging from 1.5 to 3 rad s^{-1}.

The vortex is created by rotating impulsively a 10×60 cm^2 aluminium flap in the fluid initially at rest, using a computer controlled step-motor. This flap motion generates a two-dimensional shear layer around the flap which detaches at the sharpened edge of the flap, and rolls up into a very laminar vortex. The motion profile of the flap was chosen carefully to obtain a nearly Gaussian vortex and was defined by imposing the angular velocity of the flap as a function of its angle as:

$$\dot{\Theta} = \dot{\Theta}_{max} \frac{0.42}{\Theta + 0.017} [1 + \exp{(-(\Theta/0.26)^{5/4})}]. \tag{2.1}$$

It consists of a rapid acceleration of the flap, followed by a gradual slow-down up to the angle of $\pi/2$ rad. The circulation of the vortex is varied by modifying the maximum angular velocity $\dot{\Theta}_{max}$ between 0.01 and 0.5 rad s^{-1}. The inclination of the vortex is obtained by tilting the flap with respect to the vertical in the initial plane of the flap: it was varied in the range 0 to 0.38 rad.

Particle image velocimetry (PIV) measurements of velocity fields were obtained by seeding the tank with Sphericel hollow glass spheres 110 P8 (Potter Industries), whose diameter ranges from 11 to 18 μm and whose density is approximately 1.1. The particles are illuminated by a luminous sheet of 3–5 mm thickness, created by a continuous 5 W argon-ion laser. Image pairs are recorded by a digital PIV camera (Kodak Megaplus Es 4.0) with a resolution of 2048×2048 pixels and treated by a cross-correlation algorithm developed for flows with high-velocity gradients at the laboratory (Meunier & Leweke 2003). PIV measurements have been made in three different planes (figure 2). The first one is perpendicular to the vortex axis and provides the horizontal characteristics of the initial vortex. The two other planes correspond to two orthogonal longitudinal planes, one plane being vertical ($\theta = 0$) and the other being tilted ($\theta = \pi/2$). These instantaneous two-dimensional velocity fields are extremely useful for the study of the instability since they permit us to follow the evolution of the vortex in time, which would be impossible using a two-dimensional reconstruction of point measurements.

Shadowgraph visualizations were also carried out, to observe the two-dimensional and three-dimensionl spatial distribution of density inside the vortex. For this purpose, the stratified fluid is illuminated by a large beam of parallel light, created by an intense
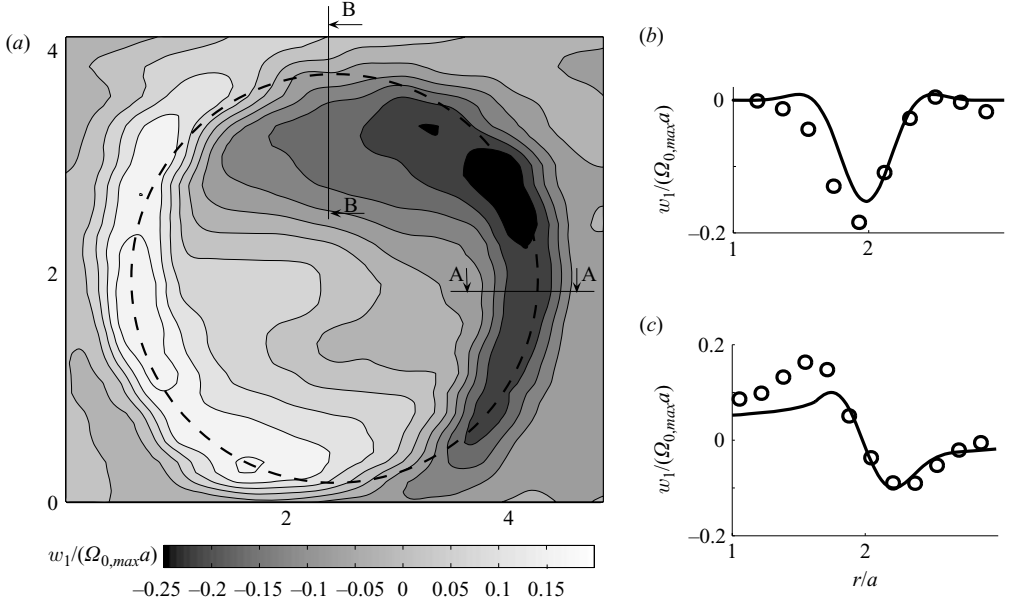
FIGURE 3. (*a*) Theoretical contours of the axial velocity of a tilted vortex in a transverse plane. (*b*, *c*) Theoretical (solid line) and experimental (circles) axial velocity profiles in two different longitudinal planes, (*b*) section A–A: $\theta = 0$, (*c*) section B–B: $\theta = \pi/2$. (*a*) The dashed line indicates the location of the critical layer. $Re = 450$, $F = 3.2$, $\alpha = 0.07$ rad.

light placed behind a small diaphragm located 2 m away from the tank. By placing a large lens (of diameter 30 cm and of focal distance 50 cm) behind the tank, it is thus possible to obtain an image of the density distribution. These images are recorded by a 2000×2000 pixel greyscale camera located behind the focal point of the lens. A small disk of 1 mm diameter was positioned exactly at the focal point of the lens, which enhances the contrast of the images.

2.2. *Characteristics of the tilted vortex*

The vortex is completely defined by its profile of angular velocity, which is very close in our experiments to the profile of a Gaussian (Lamb–Oseen) vortex:

$$\Omega_0(r) = \frac{v_\theta(r)}{r} = \frac{\Gamma}{2\pi r^2}(1 - \exp(-r^2/a^2)). \tag{2.2}$$

In our experiments, the circulation Γ was varied between 17 and 42 cm^2 s^{-1}. The core size a is slowly varying with time between 0.9 and 1.1 cm owing to viscous effects, but this dependency can be neglected on the time scale of the instability we shall describe below.

In Boulanger *et al.* (2007), it was shown that tilting the vortex with respect to the direction of stratification with an angle α creates a critical layer at the radius r_c where the angular velocity of the vortex $\Omega_0(r)$ is equal to the Brunt–Väisälä frequency. This critical layer is observed for moderate Froude numbers larger than 1 only, such that the critical radius r_c exists ($\Omega_0(r=0) > N$) and is located not too far from the vortex centre ($\Omega_0(r=0) < 5N$).

The axial velocity field created by tilting the vortex is plotted in figure 3(*a*) and compared with the viscous critical-layer profiles in figure 3(*b*, *c*). These figures are similar to those presented in Boulanger *et al.* (2007) with a minor modification to

the velocity profiles: they have been enlarged around the critical layer. This velocity field exhibits a complex spatial structure: in the vertical longitudinal plane ($\theta = 0$), the axial velocity has a jet-like profile (see figure 3b); in the tilted longitudinal plane, it looks like a shear layer (see figure 3c). There is a good agreement between theory and experiment on the structure and amplitude of the velocity field, although there are some large uncertainties (of the order of 50%) for $r < r_c$ owing to the deformation of the images by a strong refraction at the critical layer. The theory predicts that the size of the critical layer scales as $Re^{-1/3}$ and the amplitude of the density and the vertical velocity scale as $\alpha Re^{1/3}$. This leads to a scaling of the azimuthal vorticity as $\alpha Re^{2/3}$.

In the following, we will non-dimensionalize lengths by the vortex core size a. Moreover, the inverse of the angular velocity at the centre of the vortex $\Omega_0(r=0) = \Gamma/2\pi a^2$ will be used as the time scale of the flow. This leads to non-dimensionalize velocities by $\Gamma/2\pi a$. Finally, we will non-dimensionalize densities by the density of the fluid ρ_f at $z=0$. Our system is thus characterized by five non-dimensional parameters. The inclination angle α is varied from 0 to 0.38 rad. The Reynolds number $Re = \Gamma/(2\pi\nu)$ (ν being the kinematic viscosity) is varied between 160 and 800. The Froude number $F = \Gamma/(2\pi a^2 N)$ ranges from 1.5 to 4.3. The Schmidt number $Sc = \kappa/\nu$ is close to 700. The last parameter L compares the vertical stratification length to the vortex core size: $L = \rho/(a\partial\rho/\partial z)$. In our experiments, this Boussinesq parameter ranges between 100 and 400, which justifies the use of the Boussinesq approximation obtained by assuming L infinite.

3. Three-dimensional instability

3.1. *Dye visualizations*

For high Reynolds numbers, the vortex was found to be unstable with respect to a three-dimensional perturbation. The time-sequence of figure 4 shows the temporal evolution of the tilted vortex by shadowgraph visualizations. The vortex is viewed from the side perpendicularly to the tilting plane. This view reveals the density structures in the vertical plane ($\theta = 0$). The vortex is thus tilted with an angle of 0.07 rad on the images.

At the beginning, just after the end of the flap motion (figure 4a), the vortex is cylindrical and contains two strips created by the critical layer. At $t = 1$ s, these strips are subject to a sinusoidal undulation (figure 4b), which breaks the invariance along the axis of the vortex. This perturbation is initially confined within the strips. At later stages (figure 4c, d), the perturbation grows and becomes visible all around the vortex. This is due to an increase of the contrast associated with the increase of $\partial^2\rho/\partial z^2$ and not to a propagation of the perturbation around the vortex, as is attested by other visualizations made from different view angles. The undulation of the two strips is then amplified and gives birth to structures characteristic of vortices rotating in the clockwise direction (figure 4d). The two alleys of vortices alternate on each side of the vortex and the vortex centres are linked by two strips which create a zigzag-like structure. This perturbation thus looks like a secondary spiral vortex which is rolled-up around the tilted vortex in a helical mode. However, this is not the case, because it would create vortices of opposite sign on each side of the vortex. On the contrary, it can be seen clearly in figure 4(d) that the vortices are clockwise (negative vorticity in this plane) on both sides of the vortex. It is thus a perturbation which grows almost independently on both sides of the vortex. All of this suggests that the instability is localized in the critical layer, and not influenced by the global
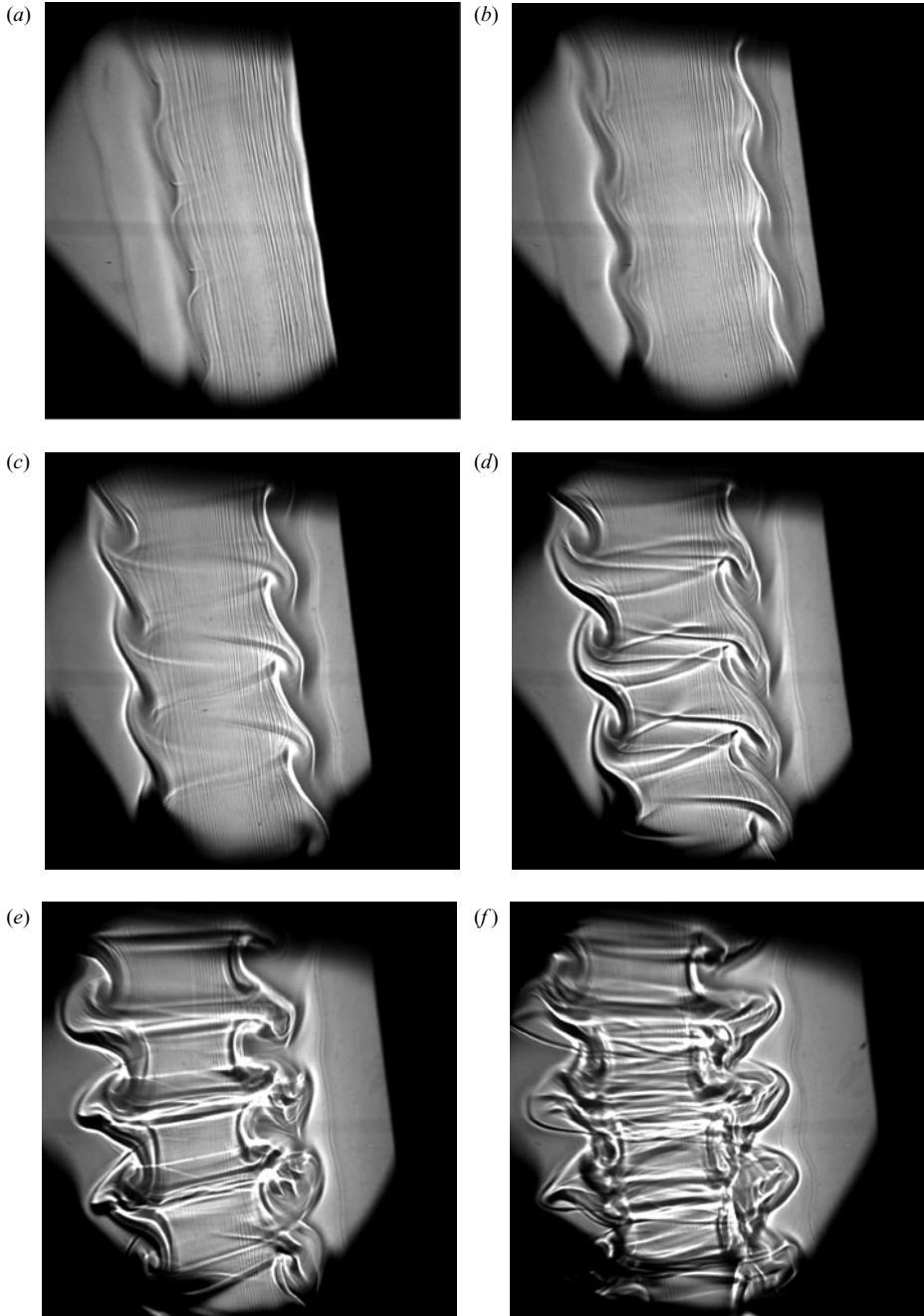
FIGURE 4. Shadowgraph sequence of the vortex instability in a vertical longitudinal plane ($\theta = 0$). The time interval is 1.1 rotation period. $F = 3$, $Re = 720$, $\alpha = 0.07$ rad. A movie of the same instability, obtained for slightly lower Reynolds and Froude numbers, is available with the online version of the paper.

structure of the vortex. These shadowgraph visualizations are very similar to the pictures presented by Cariteau (2005), and we suspect that it is the same instability that they observed although they did not tilt the generating plate.
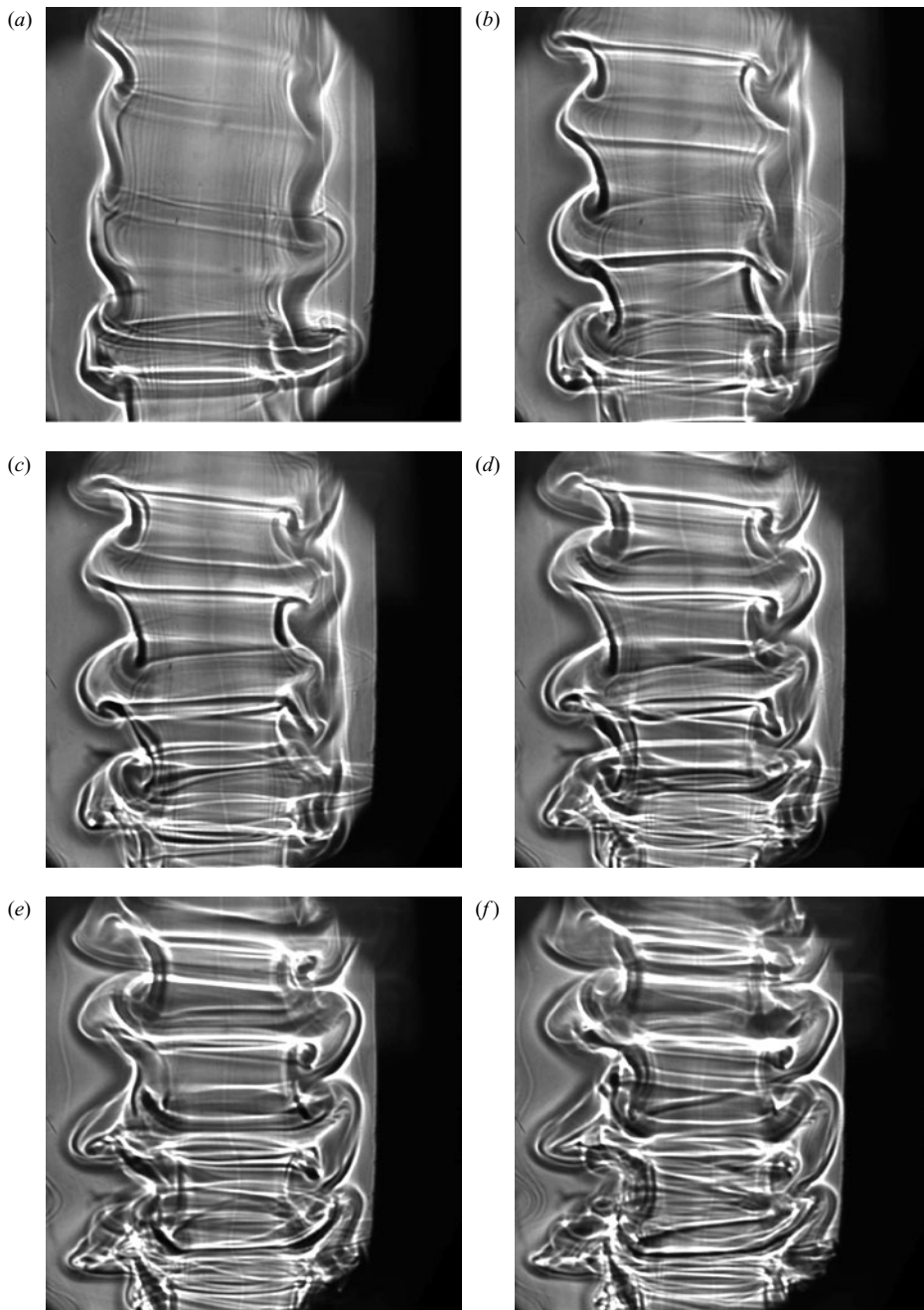
(*a*) (*b*)

(*c*) (*d*)

(*e*) (*f*)

FIGURE 5. Shadowgraph sequence of the vortex instability in a tilted longitudinal plane ($\theta = \pi/2$). The time interval is 1.1 rotation period. $F = 3$, $Re = 720$, $\alpha = 0.07$ rad.

At late stages, the instability saturates and the co-rotating vortices finally break down, leading to a strong mixing, in which some coherent structures are still visible.

Figure 5 shows the temporal evolution of the vortex in the tilted plane ($\theta = \pi/2$). Although the perturbation starts as an undulation of the critical layer (figure 5a) as in figure 4, the perturbation is then rather different. It rapidly creates an alley of

alternate vortices on each side of the vortex (figures 5*b–d*). The instability thus looks like a centrifugal instability, although the vortex is stable with respect to the Rayleigh criterion. In fact, the structure of the instability is very similar to a von Kármán vortex street on each side of the vortex. This could be related to the presence of a jet in the critical layer.

In this section, the shadowgraph visualizations were used to reveal the spatial structure of the density field from which the velocity field was inferred. However, it is not clear that the density field is simply advected by the velocity field, and there might be a three-dimensional perturbation of the density without any perturbation of the velocity field. To confirm the validity of the previous arguments, we provide in the following sections some PIV measurements, which give directly the velocity field in these longitudinal planes.

3.2. *PIV measurements*

The time-sequence of figure 6 shows the temporal evolution of the azimuthal vorticity in the tilted plane (i.e. $\theta = \pi/2$) obtained by PIV measurements. In this plane, the tilted vortex creates two critical layers on each side of the vortex, containing some strong negative (black) vorticity (see figure 6*a*). This corresponds to the vorticity of the shear layer created by tilting (see figure 3*c*). In fact, each critical layer is made of one band of strong negative vorticity, surrounded by two smaller bands of weak positive vorticity which are hardly visible on figure 6(*a*, *b*). At the vortex centre, the vorticity field contains large errors, which are due to the presence of many spurious vectors. This is caused by the images being blurry at the vortex centre owing to large deviations of the luminous rays by the critical layer.

The perturbation appears at first as a periodic modulation of the negative vorticity layers on both sides of the vortex (figure 6*b*, *d*). The instability does not induce any motion in the vortex core: it is clearly localized in the critical layer. The perturbation then leads to the formation of co-rotating vortices of negative vorticity (figure 6*e*, *f*). The wavelength is similar on both sides and the two alleys of vortices are alternate, as was observed on the shadowgraph visualizations of figure 4. The positive layers are only slightly modified by the perturbation: they split into weak vortices under the influence of the negative-layer evolution. It can be noted that these vortices are created extremely rapidly, in approximately half a rotation period $2\pi/\Omega_0(r)$ between figures 6(*b*) and 6(*e*).

The presence of an alley of co-rotating vortices is characteristic of the shear instability leading to Kelvin–Helmholtz billows at late stages. This explains why the vortices rotate in the same direction on both sides of the vortex in the visualizations of figure 4. It is thus a possible explanation of the instability. However, it is curious to see that the structure observed on the velocity field of the tilted plane ($\theta = \pi/2$) is observed on the visualizations of the vertical plane ($\theta = 0$) and not on the visualizations of the tilted plane. In fact, the density structures are advected by the velocity field and the amplitude of the density perturbation is thus maximal at the end of the forcing by the velocity perturbation, i.e. a quarter of a turn later.

At late stages, the growth stops, and the structures lose their coherence, leading to a partial reformation of the vorticity layers (see figure 6*g*). This non-uniform vorticity layer sometimes creates again some isolated vortices, but the flow is found to be less organized and very turbulent.

Figure 7 shows the azimuthal vorticity obtained by PIV measurements in the vertical plane (i.e. $\theta = 0$). The temporal evolution of the vorticity could not be obtained because the vortex slowly moves inside the water tank and a fixed measurement plane
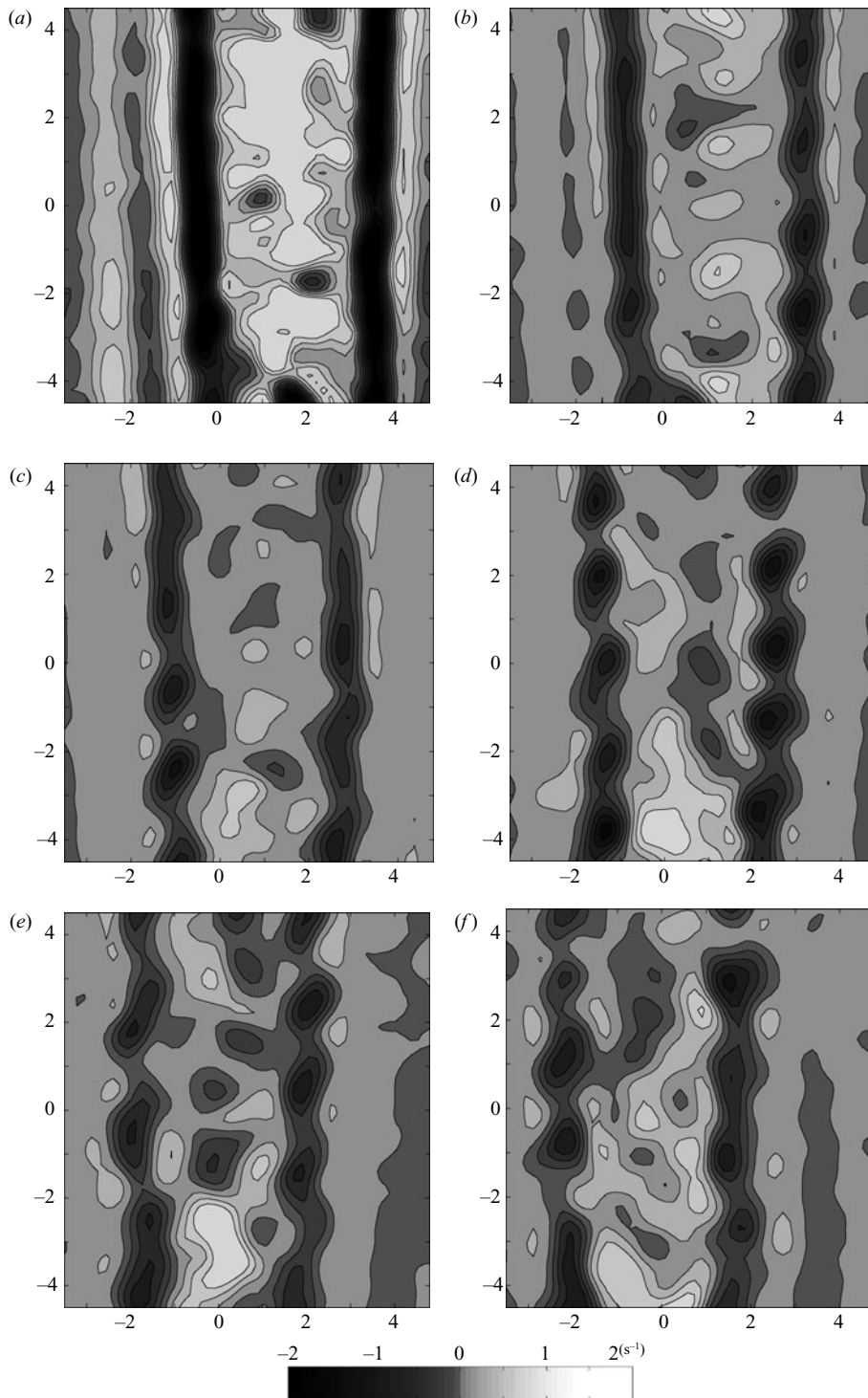
FIGURE 6. PIV sequence of the instantaneous azimuthal vorticity field in a tilted longitudinal plane ($\theta = \pi/2$), starting 10 rotation periods after the flap motion. The time interval is 0.5 rotation period. $F = 2.1$, $Re = 560$, $\alpha = 0.12\,\text{rad}$.
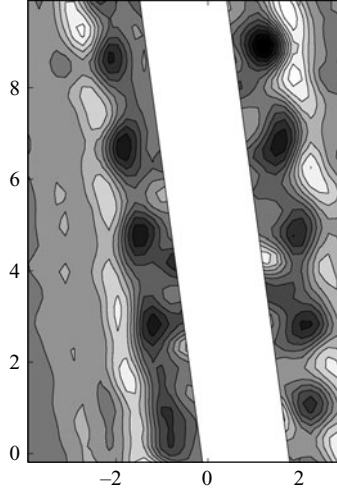
FIGURE 7. PIV measurement of the instantaneous azimuthal vorticity field in a vertical longitudinal plane ($\theta = 0$), approximately 12 rotation periods after the flap motion. $F = 2.1$, $Re = 560$, $\alpha = 0.12$ rad.

contains the axis of the vortex only at one instant in time. The centre of the vortex was masked because it contains many spurious vectors (as in figure 6), owing to the refraction of the luminous rays when they cross the critical layer.

In this vertical plane, the tilted vortex creates a jet on each side of the vortex. Each jet creates two vertical layers of opposite vorticity. Figure 7 shows that the perturbation is made of a periodic modulation of each vorticity layer, which creates an alley of alternate counter-rotating vortices. This is characteristic of the sinuous instability of a jet. This structure can be linked to the structure of the perturbation observed on the shadowgraph visualization of figure 5. However, it is again surprising to see that these structures are not observed in the same plane for the velocity field. As in the case of the Kelvin–Helmholtz instability, it can be explained by the density being advected by the vortex.

3.3. *A local instability*

The dye visualizations and the PIV measurements have shown that the instability is localized in the critical layer and that it does not modify the vortex core. Moreover, this instability appears rapidly compared to the advection time around the vortex. These two arguments mean that the instability is linked to the local properties of the critical layer rather than to the global structure of the vortex itself. This will justify the local stability analysis of the critical layer in the next section. Figure 8 shows the structure of the instability. The velocity profiles are plotted for each plane inside the critical layer and the secondary vortices are represented by spirals as would be obtained by the roll-up of a line of dye.

The critical layer has a complex structure and several instabilities are thus candidates. In the tilted plane ($\theta = \pi/2$), the velocity profile contains a strong shear and is subject to the Kelvin–Helmholtz instability. In the vertical plane ($\theta = 0$), the velocity profile is a jet-like profile and is subject to jet instabilities. Moreover, in the tilted plane, there is a strong density layer which, added to the centrifugal force, could lead to a Rayleigh–Taylor instability. This last instability would also lead to an undulation of the critical layer, as in the visualizations.
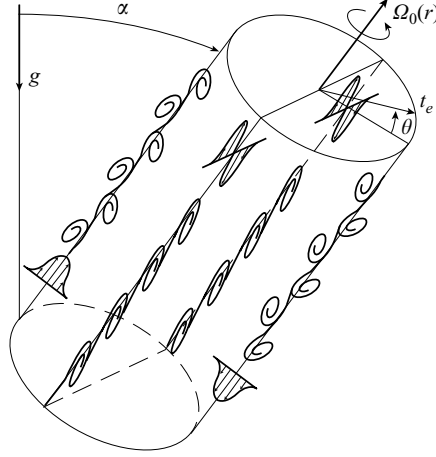
FIGURE 8. Schematic of the tilt-induced instabilities occurring in the critical layer of the vortex: a shear instability for $\theta = \pm \pi/2$ and a jet instability for $\theta = 0$ and $\theta = \pi$.

In order to determine which mechanism is responsible for the instability observed in the tilted vortex, we must evaluate the growth rate associated with each of these possible instabilities. Moreover, it is also important to quantify in which conditions the local instability can be sufficiently strong not to be affected by the mean angular advection around the vortex. The next section addresses these issues theoretically.

4. Stability analysis of the viscous critical-layer solution

In this section, we provide a theoretical analysis of the dynamics of the tilted vortex. As demonstrated in Boulanger *et al.* (2007), it is convenient to analyse the flow with new coordinates where x is modified into $x - \tan\alpha z$, and y and z are unchanged in such a way that in each horizontal plane $z = \text{const}$ the point $x = y = 0$ corresponds to the vortex centre. With these variables, the governing equations for the velocity $\boldsymbol{u} = (u, v, w)$, pressure p and density ρ are in cylindrical coordinates:

$$\frac{\mathrm{D}u}{\mathrm{D}t} - \frac{v^2}{r} - w\tan\alpha\frac{\partial u}{\partial x} - w\frac{\tan\alpha\sin\theta}{r}v = -\frac{1}{\rho}\frac{\partial p}{\partial r} + \frac{1}{Re}(\Delta\boldsymbol{u})_r, \quad (4.1a)$$

$$\frac{\mathrm{D}v}{\mathrm{D}t} + \frac{uv}{r} - w\tan\alpha\frac{\partial v}{\partial x} + w\frac{\tan\alpha\sin\theta}{r}u = -\frac{1}{\rho r}\frac{\partial p}{\partial\theta} + \frac{1}{Re}(\Delta\boldsymbol{u})_\theta, \quad (4.1b)$$

$$\frac{\mathrm{D}w}{\mathrm{D}t} - w\tan\alpha\frac{\partial w}{\partial x} = -\frac{1}{\rho}\frac{\partial p}{\partial z} + \frac{\tan\alpha}{\rho}\frac{\partial p}{\partial x} - \frac{L}{F^2} + \frac{1}{Re}\Delta w, \quad (4.1c)$$

$$\frac{\mathrm{D}\rho}{\mathrm{D}t} - w\tan\alpha\frac{\partial\rho}{\partial x} = 0, \quad (4.1d)$$

$$\frac{1}{r}\frac{\partial(ru)}{\partial r} + \frac{1}{r}\frac{\partial v}{\partial\theta} + \left(\frac{\partial}{\partial z} - \tan\alpha\frac{\partial}{\partial x}\right)w = 0, \quad (4.1e)$$

with

$$\frac{\mathrm{D}}{\mathrm{D}t} = \left(\frac{\partial}{\partial t} + u\frac{\partial}{\partial r} + \frac{v}{r}\frac{\partial}{\partial\theta} + w\frac{\partial}{\partial z}\right) \quad (4.2a)$$

$$\frac{\partial}{\partial x} = \cos\theta\frac{\partial}{\partial r} - \frac{\sin\theta}{r}\frac{\partial}{\partial\theta}. \quad (4.2b)$$

The problem is characterized by the angle α, the Froude number F, the length ratio L and the Reynolds number Re. The diffusion of density has been neglected. Note that the gravity g is given by L/F^2 in term of these parameters.

As shown in Boulanger *et al.* (2007), a basic flow solution can be obtained in the limit of small α, large Reynolds numbers and large L in the form

$$(u_b, v_b, w_b, p_b, \rho_b) = (0, V_0(r), 0, p_0(r, z), \rho_0(r, z)) + \alpha \left(\frac{u_1}{L}, \frac{v_1}{L}, w_1, \frac{p_1}{L}, \frac{\rho_1}{L} \right) e^{i\theta} + c.c.,$$
(4.3)

where the first term represents an axisymmetric vortex, and the second term the first-order corrections in α and $1/L$ induced by tilting. This solution is singular at the critical point r_c defined by $\Omega_0(r_c) = 1/F$, and a specific approximation with a local viscous variable $\bar{r} = Re^{1/3}(r - r_c)$ was constructed in Boulanger *et al.* (2007) to describe the solution near this point. The viscous critical-layer solution was shown to exhibit strong shear which is believed to be responsible for the instability observed in the experiments. For this reason, we now perform a local stability analysis of the critical-layer solution.

As shown in Boulanger *et al.* (2007), the basic flow expands in the critical layer as:

$$u_b = \frac{\alpha}{L Re^{1/3}} \mathrm{Re}[\bar{u}_1(\bar{r}, \theta)],$$
(4.4a)

$$v_b = V_{0c} + \frac{\bar{r} V'_{0c}}{Re^{1/3}} + \frac{\alpha}{L} \mathrm{Re}[\bar{v}_1(\bar{r}, \theta)],$$
(4.4b)

$$w_b = \alpha Re^{1/3} \mathrm{Re}[\bar{w}_1(\bar{r}, \theta)],$$
(4.4c)

$$p_b = \frac{\rho_{0c} L^2 e^{-z/L}}{F^2} \left(1 + \frac{\alpha F^2}{L^3} \mathrm{Re}[\bar{p}_1(\bar{r}, \theta)] \right),$$
(4.4d)

$$\rho_b = \rho_{0c} e^{-z/L} \left(1 + \frac{\alpha Re^{1/3}}{L} \mathrm{Re}[\bar{\rho}_1(\bar{r}, \theta)] \right),$$
(4.4e)

where we have kept the first-order terms in α and $1/L$ only. In these expressions, V_{0c} and V'_{0c} are defined as the azimuthal velocity and its derivative at r_c. The functions $\bar{u}_1$, $\bar{v}_1$, $\bar{p}_1$ and $\bar{\rho}_1$ are connected to the critical-layer solution

$$\bar{w}_1(\bar{r}, \theta) = \frac{\pi r_c}{F^2 |2\Omega'_{0c}|^{2/3}} \mathrm{Hi} \left(i|2\Omega'_{0c}|^{1/3}\bar{r} \right) e^{i\theta} \,,$$
(4.5)

via the relations

$$\bar{\rho}_1 = -iF\bar{w}_1 \,,$$
(4.6a)

$$\frac{d\bar{p}_1}{d\bar{r}} = -\frac{rc\bar{\rho}_1}{F^2} \,,$$
(4.6b)

$$\bar{v}_1 = -\frac{F\bar{p}_1}{r_c} \,,$$
(4.6c)

$$\frac{d\bar{u}_1}{d\bar{r}} = -i\frac{\bar{v}_1}{r_c} \,.$$
(4.6d)

The function Hi appearing in (4.5) is the Scorer's function (see Abramowitz & Stegun 1965, p. 448) and Ω'_{0c} is the derivative of the angular velocity at r_c. The theoretical profiles plotted in figures 3(b) and 3(c) for $\theta = 0$ and $\theta = \pi/2$ correspond to the real part and imaginary part of (4.5), respectively.

As the base flow varies on a $Re^{-1/3}$ radial length scale in the critical layer, it is natural to search three-dimensional perturbations varying on a similar axial length scale and

thus to introduce a new axial variable $\bar{z} = Re^{1/3}z$. However, the angular variation of the base flow is weak and no high azimuthal wavenumber perturbation has been observed in the experiments. Therefore, we shall consider only small azimuthal wavenumber perturbations.

In the limit of small α, large Reynolds numbers and large length ratio L, the perturbation equations obtained by linearizing the system (4.1*a*)–(4.1*e*) around the local base flow (4.4*a*)–(4.4*e*) can then be reduced into the following form:

$$\left(\frac{\partial}{\partial t} + \frac{1}{F}\frac{\partial}{\partial \theta} + \mathrm{Re}(\bar{w}_1)\alpha Re^{2/3}\frac{\partial}{\partial \bar{z}} \right) u - 2\frac{v}{F} = -\frac{\partial p}{\partial \bar{r}}, \tag{4.7a}$$

$$\left(\frac{\partial}{\partial t} + \frac{1}{F}\frac{\partial}{\partial \theta} + \mathrm{Re}(\bar{w}_1)\alpha Re^{2/3}\frac{\partial}{\partial \bar{z}} \right) v + \omega_{0c}u = 0, \tag{4.7b}$$

$$\left(\frac{\partial}{\partial t} + \frac{1}{F}\frac{\partial}{\partial \theta} + \mathrm{Re}(\bar{w}_1)\alpha Re^{2/3}\frac{\partial}{\partial \bar{z}} \right) w + \alpha Re^{2/3}\mathrm{Re}(\bar{w}_1')u = -\frac{\partial p}{\partial \bar{z}} - \frac{\rho}{F^2}, \tag{4.7c}$$

$$\left(\frac{\partial}{\partial t} + \frac{1}{F}\frac{\partial}{\partial \theta} + \mathrm{Re}(\bar{w}_1)\alpha Re^{2/3}\frac{\partial}{\partial \bar{z}} \right) \rho + \alpha Re^{2/3}\mathrm{Re}(\bar{\rho}_1')u - w = 0, \tag{4.7d}$$

$$\frac{\partial u}{\partial \bar{r}} + \frac{\partial w}{\partial \bar{z}} = 0 . \tag{4.7e}$$

The $O(Re^{-1/3})$ viscous forces, the $O(1/L)$ non-Boussinesq effects and the $O(\alpha Re^{1/3})$ advection terms of the base flow correction by the azimuthal velocity of the perturbation, are all negligible with respect to the dominant $O(1)$ or $O(\alpha Re^{2/3})$ advection terms associated with the main rotation or the axial velocity field induced by tilting. The $O(\alpha/L)$ radial buoyancy force induced by the radial variation of the density, which is responsible for the Rayleigh–Taylor instability, is also negligible.

The above system of equations is complicated because it is inhomogeneous with respect to both $\bar{r}$ and θ. Local perturbations are advected around the vortex and modified during their angular rotation owing to the dependency of $\bar{w}_1$ and $\bar{\rho}_1$ on θ. Yet, the experimental observations discussed in the previous section tend to demonstrate that the characteristics of the perturbations are mainly associated with the local axial velocity profile, and that its growth results from a local process. In other words, angular advection of the perturbation by the vortex is expected to be small during the growth of the perturbation. This amounts to neglecting the term $F^{-1}\partial_\theta$ in the (4.7*a*)–(4.7*d*) in front of $\alpha Re^{2/3}$. This hypothesis has several consequences. The terms $-2v/F$ in (4.7*a*), $\omega_{0c}u$ in (4.7*b*), ρ/F^2 in (4.7*c*) and w in (4.7*d*) also become negligible. This means that if the dynamics of the perturbations is not affected by the angular advection, it is neither affected by vertical stratification nor Coriolis effects in these dimensionless variables. However, the instability is indirectly related to the stratification through the position and amplitude of the critical layer (which define the dimensionless variables). The perturbation then follows the dynamics of two-dimensional perturbations in a parallel unstratified shear flow $\alpha Re^{2/3}\bar{w}_1(\bar{r}, \theta)$ where θ can be considered as a parameter.

If we normalize spatial and time variables by

$$\delta_c = \frac{1}{|\Omega_{0c}'Re|^{1/3}}, \tag{4.8a}$$

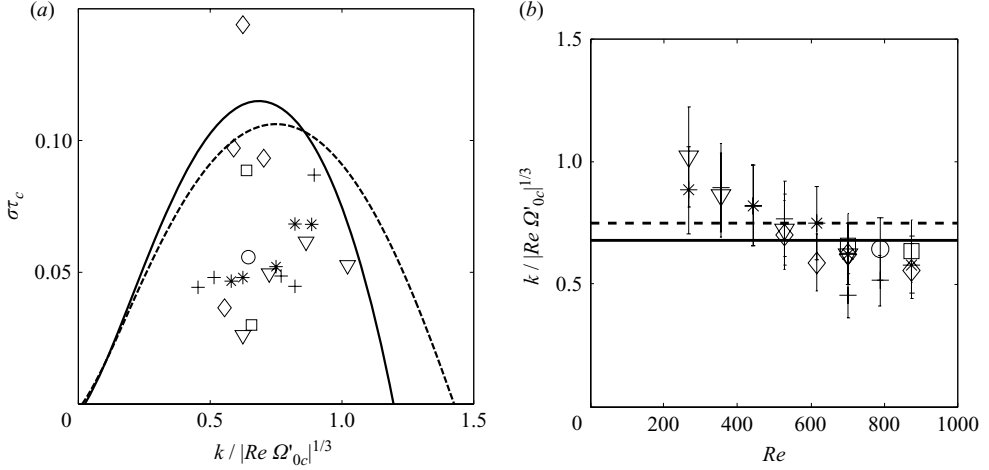$$\tau_c = \frac{|\Omega_{0c}'|^{1/3}F^2}{r_c\alpha Re^{2/3}}, \tag{4.8b}$$

FIGURE 9. (a) Maximum growth rate versus the axial wavenumber of the most unstable mode. (b) Most unstable wavelength as a function of the Reynolds number. The theoretical lines correspond to a jet profile ($\theta = 0$) for a dashed line and to a mixing layer profile ($\theta = \pi/2$) for the solid line. Experimental data have been obtained for $\alpha = 0.03$ rad ($\circ$), $\alpha = 0.07$ rad ($\square$), $\alpha = 0.14$ rad ($\diamond$), $\alpha = 0.23$ rad ($+$), $\alpha = 0.30$ rad ($*$), $\alpha = 0.38$ rad ($\triangledown$).

such that

$$\tilde{r} = \bar{r}|\Omega'_{0c}|^{1/3} = (r - r_c)/\delta_c, \tag{4.9a}$$

$$\tilde{z} = \bar{z}|\Omega'_{0c}|^{1/3} = z/\delta_c, \tag{4.9b}$$

$$\tilde{t} = t/\tau_c, \tag{4.9c}$$

$$\tilde{w}_1 = \alpha Re^{1/3} \bar{w}_1 \tau_c/\delta_c = \mathrm{Re}\left(\frac{\pi}{2^{2/3}} \mathrm{Hi}\left(2^{1/3}\tilde{r}\right) \mathrm{e}^{\mathrm{i}\theta}\right), \tag{4.9d}$$

a familiar Rayleigh equation,

$$(-\mathrm{i}\tilde{\omega} + \mathrm{i}\tilde{k}\tilde{w}_1)\left(\frac{\partial^2}{\partial \tilde{r}^2} - \tilde{k}^2\right)\tilde{u} + \mathrm{i}\tilde{k}\tilde{w}''_1 \tilde{u} = 0, \tag{4.10}$$

is obtained for the radial velocity amplitude $\tilde{u}$ of the normal mode $u(\tilde{r}, \tilde{z}, \tilde{t}) = \tilde{u}(\tilde{r})\mathrm{e}^{\mathrm{i}\tilde{\omega}\tilde{t} - \mathrm{i}\tilde{k}\tilde{z}}$.

The maximum growth rate $\mathrm{Im}(\tilde{\omega})$ versus $\tilde{k}$ of the perturbation to the profile $\tilde{w}_1$ is plotted in figure 9 for $\theta = 0$ and $\theta = \pi/2$. We recall that $\theta = 0$ corresponds to the vertical plane in which $\tilde{w}_1$ has a jet profile (figure 3b). The other value $\theta = \pi/2$ corresponds to the tilted plane in which $\tilde{w}_1$ has a mixing layer profile (figure 3c). As expected, the local mixing-layer profile is slightly more unstable than the jet, and classical results of stability are recovered (see Drazin & Reid 1981). The most unstable mode of the mixing layer is stationary with a growth rate

$$\mathrm{Im}\left(\tilde{\omega}_{ML}^{max}\right) = \sigma_{ML}^{max}\tau_c \approx 0.12, \tag{4.11}$$

reached for

$$\tilde{k}_{ML}^{max} = k_{ML}^{max}\delta_c \approx 0.68. \tag{4.12}$$

The most unstable mode of the jet is a sinuous mode with

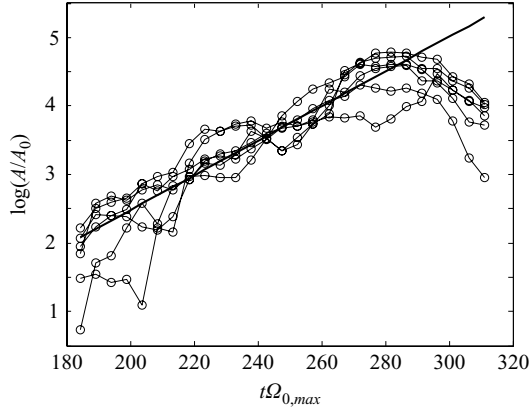$$\tilde{k}_J^{max} = k_J^{max}\delta_c \approx 0.75. \tag{4.13}$$

FIGURE 10. Evolution of the amplitude of the perturbations from shadowgraph visualizations for $Re = 700$, $F = 3.8$ and $\alpha = 0.23$ rad.

This mode has a growth rate

$$\mathrm{Im}\left(\tilde{\omega}_J^{max}\right) = \sigma_J^{max}\tau_c \approx 0.11, \tag{4.14}$$

and contrarily to the mixing-layer mode, it is propagating with a phase velocity

$$c_J \frac{\tau_c}{\delta_c} \approx 0.24 \ . \tag{4.15}$$

Experimental estimates for the growth rate have also been added in figure 9. They have been obtained from shadowgraph visualizations in the vertical longitudinal plane. For this purpose, the amplitude of the sinusoidal undulation of the critical layer was measured manually on two wavelengths on each side of the vortex. This leads to 10 determinations of the amplitude of the perturbation as a function of time. They are plotted in figure 10 where the uncertainty can be as large as 20%. In this figure, the amplitude increases exponentially, which leads to the determination of the growth rate. However, these growth rate measurements contain a large uncertainty for various reasons. First, the advection of the structures around the vortex can drastically increase or decrease the growth of the amplitude if the perturbation is not homogeneous in θ. Secondly, there is a competition between several wavelengths, which makes it hard to follow exactly the same maximum and minimum of the undulation. All of this induces a large uncertainty in the determination of the growth rate, whose error can be as large as 50%.

Figure 9(a) shows that the growth rates measured experimentally are, in general, smaller than the theoretical predictions and can be as small as half the theoretical value. This is not surprising because the theory does not take into account the stabilizing viscous and advection effects. Moreover, as explained above, the presence of various wavelengths might introduce a small bias toward smaller values during the experimental determination of the growth rate. Figure 9(b) shows the measured wavelength as a function of the Reynolds number. It is very close to the theoretical value of the maximum growth rate. The results are apparently slightly dependent on the Reynolds number, showing that smaller wavelengths are obtained for larger values of the Reynolds number. This is surprising because viscosity is expected to damp preferentially the smaller wavelengths. Further data are required in order to confirm this slight dependency.
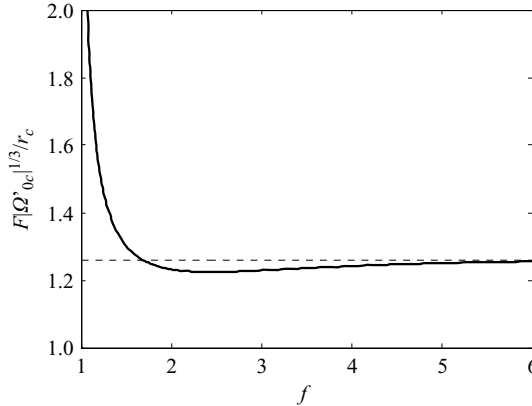
FIGURE 11. Variation of the amplitude factor of the local growth rate: $r_c/(F|\Omega'_{0c}|^{1/3})$ versus F. The dashed line is the asymptotic value $2^{1/3}$ obtained for large F.

For large Froude numbers, a theoretical estimate for τ_c can be obtained. In this limit, the critical layer is far from the vortex centre in a region where $\Omega_0(r) \sim 1/r^2$. The critical radius r_c and Ω'_{0c} can therefore be expressed in terms of F such that we obtain $(F|\Omega'_{0c}|^{1/3}/r_c) \approx 2^{1/3}$ for large F. By plotting $(F|\Omega'_{0c}|^{1/3}/r_c)$ versus F (see figure 11), we can see that this estimate applies approximatively as soon as $F > 1.5$. It follows that $\tau_c \sim F/(2^{1/3}\alpha Re^{2/3})$ for $F > 1.5$. The consequence is that the product $\sigma_{ML}^{max}F$, which compares the maximum growth rate to the angular advection frequency, becomes independent of the Froude number. It is given (for $F > 1.5$) by

$$\sigma_{ML}^{max}F \approx 0.1\alpha Re^{2/3}. \tag{4.16}$$

A priori, the theory requires that this product must be large, which means

$$\alpha Re^{2/3} \gg 10. \tag{4.17}$$

Figure 12 shows the experimental stability diagram of the tilt-induced instability. Three types of behaviour have been observed. For high Reynolds numbers and high tilt angles, the flow presents the instability described previously. The corresponding parameter region has been marked as light grey in figure 12. As predicted by the theory, this instability appears for Froude numbers larger than 1 and for $\alpha Re^{2/3}$ sufficiently large. When the Froude number is smaller than 1, the critical layer disappears and no instability was observed. When the parameter $\alpha Re^{2/3}$ becomes small (of the order of 5), we have observed that the critical-layer establishment is followed by the development of non-stationary and non-persistent disturbances. After the disappearance of the disturbances, the critical layer starts to beat at the Brunt–Väisälä frequency. This regime is indicated in dark grey in figure 12. It is found for $\alpha Re^{2/3}$ decreasing from 10 to 3 when the Froude number increases from 1 to 4. It is not clear whether this region tends to $\alpha Re^{2/3} = 0$ for larger Froude numbers. We have not been able to explore this domain of parameters because it corresponds to very small tilt angles which are too strongly affected by the remnant motions of the fluid in the tank.

5. Late stages

We have also analysed the evolution of the tilted vortex when the instability is strongly active. PIV measurements were made in a horizontal plane in order to study
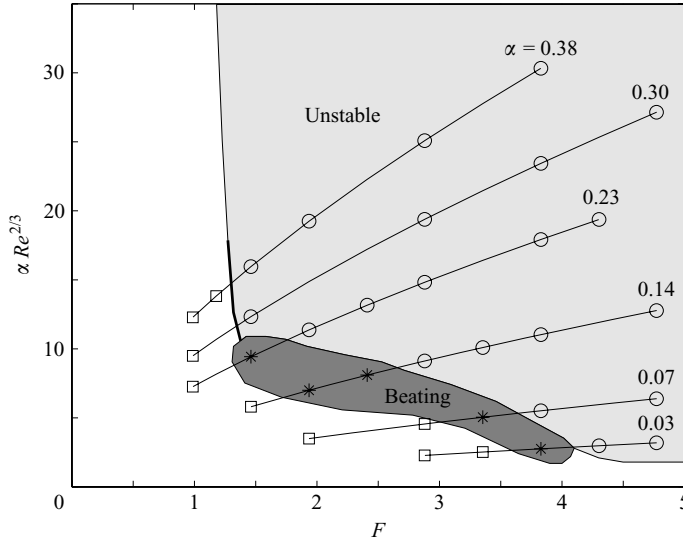
FIGURE 12. Experimental stability diagram of the tilt-induced instability for various inclination angles α of the vortex. Each experiment can present a stable flow ($\square$), an unstable flow ($\circ$) or a beating of the perturbation ($*$).

the two-dimensional characteristics of the final vortex. The two-dimensional velocity fields show that the vortex remains very close to axisymmetric and that the mean velocity profile is fitted very well by the profile of a Gaussian vortex defined by (2.2). The circulation and the core size were thus evaluated as a function of time for three different tilt angles and for two different Reynolds numbers by fitting the experimental data with the Gaussian vortex.

The circulation Γ of the vortex is shown in figure 13(*a*) as a function of time. The uncertainty is very small, but it may depend slightly on the method used for the fit of the experimental data. The overall error is smaller than 5%. The dotted symbols correspond to a vertical vortex (used as a reference), for which the circulation remains constant after a vortex formation time of approximately 5 s. Open symbols show the results of a vortex tilted with an angle $\alpha = 0.12$ rad. For this tilt angle, the three-dimensional perturbation appears around $t = 9$ s for both Reynolds numbers. The circulation is roughly constant, although it increases by about 30% for the smaller Reynolds number and decreases by about 15% for the larger Reynolds number. The vortex is not broken by the instability, even though the instability is very active. This is consistent with Kelvin's theorem predicting that the circulation should be conserved. The small variations of the circulation are probably due to slight modifications of the vortex profile during the instability.

The square of the core size a^2 is plotted in figure 13(*b*) as a function of time. The uncertainty for this parameter is slightly larger than for the circulation: the error can be as high as 10% for the tilted vortex owing to strong refractions in the turbulent regions. For a vertical vortex, it increases linearly with time owing to viscous diffusion, with a slope 4ν (shown as thick lines) corresponding to a non-stratified Gaussian vortex. For a vortex tilted with an angle $\alpha = 0.12$ rad, the initial evolution of the core size is similar, showing that the formation of the vortex is weakly influenced by the tilt angle. However, the core size jumps suddenly to a large value after the onset of the instability, when the Reynolds number is equal to 2000. This comes from the
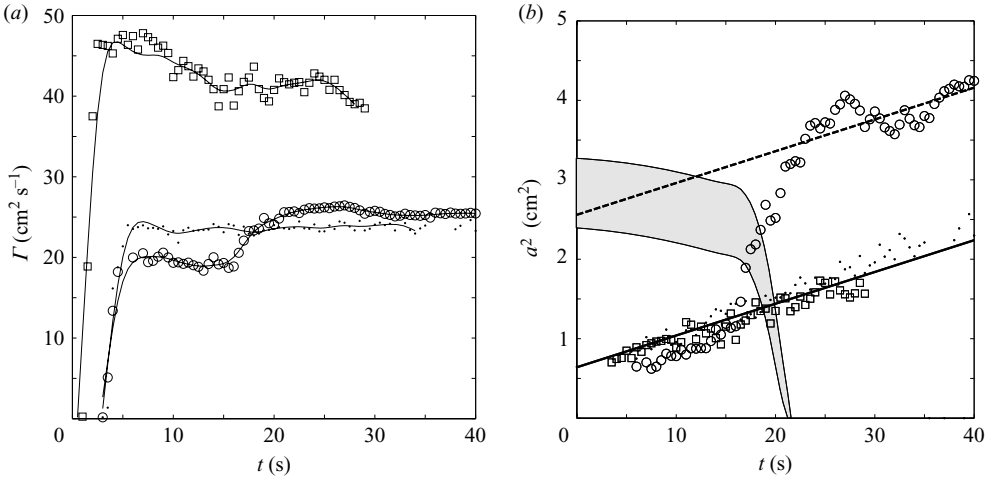
FIGURE 13. Temporal evolution of (*a*) the circulation and (*b*) the core size of a tilted vortex. Dotted symbols are the reference vertical vortex. Open symbols correspond to a tilt angle $\alpha = 0.12$ rad and a Reynolds number $Re = 2000$ (○) and $Re = 4200$ (□). (*a*) The solid lines are experimental data fits. (*b*) The slope of the lines is calculated from the viscous evolution of a Gaussian vortex and the grey area indicates the position and width of the critical layer for the $Re = 2000$ (○) experiment.

large dispersion caused by the instability which enhances the diffusion of the vorticity and creates an artificial growth of the core size. The final vortex has a core size 50% larger than in the absence of instability. Such a sudden increase of the core size has not been observed for a higher Reynolds number ($Re = 4200$) although the instability was more active there. This can be explained by the instability being located much farther from the vortex centre in that case, because the Froude number is twice as large. The position of the critical layer can be calculated for these two experiments. For the lower Reynolds number, it is indicated in figure 13(*b*) by the grey area. We can see that this region is close to the core radius when the instability develops. On the contrary, the grey area would be outside the figure for the higher Reynolds number, since it is located around $r_c^2 \approx 10\,\mathrm{cm}^2$. For the lower Reynolds number, the sudden increase of the core size induces a sudden decrease of the Froude number and a disappearance of the critical layer. This might explain why the instability saturates and creates only a beating of the flow, probably associated with the oscillation of a stable Kelvin mode. After the turbulence has slowed down, the core size seems to increase again as for a Gaussian vortex.

We can infer from these observations that at high Reynolds numbers, the instability of a tilted vortex will not break the vortex, but will increase its core size if its Froude number is close to 1.

6. Conclusion

In this paper, we have analysed the dynamics of a tilted vortex in a stratified fluid for small inclination angles, large Reynolds numbers and Froude numbers larger than 1.

In a previous paper (Boulanger *et al.* 2007), we showed that when $F > 1$, tilting induces a strong axial flow and important density variations in a cylindrical region located near a critical radius where the Brunt–Väisälä frequency is equal to the angular velocity of the vortex. Moreover, it was also shown that these corrections to

the rotating flow were captured well by a viscous critical-layer analysis: the axial flow was demonstrated to have an $m = 1$ azimuthal structure, and radial profiles which vary from jet in the vertical plane ($\theta = 0$) to mixing layer in the tilted plane ($\theta = \pi/2$). Here, we have demonstrated experimentally that the axial flow correction is responsible for a violent instability characterized by the formation of small co-rotating vortices on either side of the vortex. The growth rate and the spatial structure of the instability mode have been obtained using visualizations and PIV measurements, and compared to the theoretical predictions obtained from a local stability analysis of the radial profile of axial flow in the viscous critical layer.

A good quantitative agreement has been obtained for the wavelength of the modes supporting the hypothesis that the instability is mainly governed by the local stability characteristics for the experimental parameters we have considered. However, we have also observed that experimental estimates for the instability growth rate were up to a factor 2 below the local theoretical predictions. We have attributed this discrepancy to the large uncertainties found in the experimental measurements, to the possible bias due to the competition between several wavelengths and to neglected viscous and advection effects in the theory.

The theoretical description has permitted us to show that, as soon as $F > 1.5$, the condition for the validity of the local approach does not depend on the Froude number and only requires the product $\alpha Re^{2/3}$ to be large. This product is also expected to be the parameter controlling the stability of the tilted vortex: the dimensional growth rate is shown to be equal to $0.1 \alpha Re^{2/3} N$, N being the Brunt–Väisälä frequency. When this product is small, the local instability is in competition with the angular advection of the vortex: the vortex becomes stable because local perturbations do not have time to grow sufficiently before being advected. In our experiments, we have observed that the stability threshold was slightly Froude-number dependent: it varied from $\alpha Re^{2/3} = 10$ to $\alpha Re^{2/3} = 3$ when the Froude number increases from 1 to 4.

We have also looked at the evolution of the vortex after the development of the instability. We have observed that the instability does not break the vortex and its circulation does not change significantly. However, the instability can increase the core size of the vortex by 50% and hence decrease its Froude number below the threshold for the instability. This effect is observed only when the Froude number is small enough (between 1 and 3), such that the critical layer is close to the vortex centre.

It is striking to see that this instability occurs for tilt angles as small as 0.03 rad (2°) at high Reynolds numbers, and is thus likely to happen in most situations. We have observed that the tilt angle of the vortex could vary from at least 1° owing to the remnant motions in the tank. We suspect that it was the case in the experiments of Cariteau (2005), who observed exactly the same instability without any intentional tilt of the vortex. We thus expect this instability to occur in real geophysical flows, where the Reynolds numbers are much higher than in laboratory experiments. A consequence would be that vortices with a Froude number close to 1 are subject to this instability and will thus decrease their Froude number below 1, where the instability disappears. Such a defect of vortices with Froude number close to 1 might be visible in oceanic and atmospheric data.

Finally, it is clear that this instability creates a strong vertical mixing of the stratified fluid. This mixing mechanism is different from the simple overturning mechanism which is often invoked in the ocean (Farmer, Pawlowicz & Jiang 2002). It will be now interesting to quantify its real contribution to the global mixing properties of the ocean.

We would also like to mention that Schecter, Montgomery & Reasor (2002) have examined a situation in which a local tilting was created by a three-dimensional linear Rossby wave. In their case, a critical layer is also present, but its role is to damp the linear Rossby wave and then favour the realignment of the vortex with the direction of stratification. It is not clear what the structure of the flow is in that critical layer and whether secondary instabilities such as the one described here could develop.

REFERENCES

ABRAMOWITZ, M. & STEGUN, I. A. 1965 *Handbook of Mathematical Functions*. Dover.

BILLANT, P. & CHOMAZ, J.-M. 2000 Experimental evidence for a new instability of a vertical columnar vortex pair in a strongly stratified fluid. *J. Fluid Mech.* **418**, 167–188.

BOULANGER, N., MEUNIER, P. & LE DIZÈS, S. 2007 Structure of a stratified tilted vortex. *J. Fluid Mech.* **583**, 443–458.

CARITEAU, B. 2005 Etude de la stabilité et de l'interaction de cyclones intenses en fluide stratifié. PhD thesis, Université Joseph Fourier, Grenoble.

CARITEAU, B. & FLÓR, J.-B. 2003 Instability of a columnar vortex in stratified fluid. *Bull. Am. Phys. Soc.* **48** (10), 164.

CROW, S. C. 1970 Stability theory for a pair of trailing vortices. *AIAA J.* **8**, 2172–2179.

DRAZIN, P. G. & REID, W. H. 1981 *Hydrodynamic Stability*. Cambridge University Press.

FARMER, D., PAWLOWICZ, R. & JIANG, R. 2002 Tilting separation flows: a mechanism for intense vertical mixing in the coastal ocean. *Dyn. Atmos. Oceans* **36**, 43–58.

GARNIER, E., MÉTAIS, O. & LESIEUR, M. 1996 Instabilités primaire et secondaire d'un jet barocline. *C. R. Acad. Sci., Paris* B **323**, 161–168.

HOPFINGER, E. J. & VAN HEIJST, G. J. F. 1993 Vortices in rotating fluids. *Annu. Rev. Fluid Mech.* **25**, 241–289.

KERSWELL, R. R. 2002 Elliptical instability. *Annu. Rev. Fluid Mech.* **34**, 83–113.

MEUNIER, P. & LEWEKE, T. 2003 Analysis and optimization of the error caused by high velocity gradients in particle image velocimetry. *Exps. Fluids* **35**, 408–421.

NIEMAN, P. J., SHAPIRO, M. A. & FEDOR, L. S. 1993 The life cycle of an extratropical marine cyclone. Part ii: mesoscale structure and diagnostics. *Mon. Weather Rev.* **121**, 2177–2199.

PAWLAK, G., MACCREADY, P., EDWARDS, K. A. & MCCABE, R. 2003 Observations on the evolution of tidal vorticity at a stratified deep water headland. *Geophys. Res. Lett.* **30** (24), 2234.

POLAVARAPU, S. M. & PELTIER, W. R. 1993 Formation of small-scale cyclones in numerical simulations of synoptic-scale baroclinic wave life cycles: secondary instability at the cusp. *J. Atmos. Sci.* **50**, 1047–1057.

SCHECTER, D. A., MONTGOMERY, M. T. & REASOR, P. D. 2002 A theory for the vertical alignment of a quasigeostrophic vortex. *J. Atmos Sci.* **59** (2), 150–168.